Experimentally Characterizing the Plume of a Divergent Cusped-Field Thruster

IEPC-2009-259

Presented at the 31st International Electric Propulsion Conference,
University of Michigan, Ann Arbor, Michigan, USA
September 20–24, 2009

Stephen R. Gildea* and Manuel Martínez-Sánchez†
Massachusetts Institute of Technology, Cambridge, Massachusetts, 02139, USA

Michael R. Nakles‡ and William A. Hargus, Jr.§
Air Force Research Laboratory Spacecraft Propulsion Branch, Edwards Air Force Base, California, 93524, USA

Divergent cusped-field thrusters are electric propulsion devices characterized by a divergent, dielectric wall channel and a magnetic topology dominated by two magnetic cusps and a magnetic bottle near the anode. Initial testing results suggest that this technology may lend itself to miniaturization while providing improved lifetime performance over miniature Hall thruster designs. This paper presents results of detailed probing of the divergent cusped-field thruster plume using a Faraday cup and a retarding potential analyzer to measure the ion current density and energy distributions at varied operating conditions. These results provide a more complete experimental characterization of the plume than was previously available by measuring plume attributes at wider angles with increased spatial resolution. Plume data analyses show regions with the greatest current density contain the most energetically uniform ion populations. However, the retarding potential analyzer results indicate that highly energetic ions are expelled at large angles relative to the thruster axis of symmetry, though the current densities at these angles are much lower. Plume measurements made while varying the cathode operating condition are also presented. The operating conditions of the divergent cusped-field thruster and cathode are found to be strongly coupled, motivating a future study that systematically examines the effect of cathode location and operating condition on the performance of the thruster. Additionally, time resolved anode current measurements are presented for several operating conditions. These data reveal a distinct difference between the low and high-current modes, demonstrating that the anode current is much less oscillatory in the low-current mode than the high-current mode.

*Graduate Student, Department of Aeronautics and Astronautics, sgildea@mit.edu
†Professor, Department of Aeronautics and Astronautics, mmart@mit.edu
‡Research Engineer, ERC Inc., michael.nakles.ctr@edwards.af.mil
§Research Engineer, AFRL/RZSS, william.hargus@edwards.af.mil

The 31st International Electric Propulsion Conference, University of Michigan, USA
September 20-24, 2009

Nomenclature

R = radial coordinate of probe
Θ = angular coordinate of probe
I = ion current collected by retarding potential analyzer
e = elementary charge
A_p = effective retarding potential analyzer ion current collector area
Γ_i = ion flux to retarding potential analyzer collector
V_r = ion retarding voltage with respect to ground
ε = ion energy
f_Γ = energy distribution of ion flux
V_a = anode potential with respect to ground
I_a = anode current
$\dot{m}_a$ = anode mass flow rate
I_k = keeper current
$\dot{m}_c$ = cathode mass flow rate
V_k = keeper potential with respect to ground
I_b = ion beam current
$\Theta_{90\%}$ = half angle containing ninety percent of ion beam current

I. Introduction

STATIONARY plasma type (SPT) Hall thrusters have been operated in earth orbit since 1972[1] with typical efficiencies near 50% and a specific impulse of 1600 s.[2] However, the operational lifetime of SPT Hall thrusters is often limited by erosion of dielectric material used to provide insulation from the plasma.[3] Researchers at the Massachusetts Institute of Technology (MIT) Space Propulsion Laboratory (SPL) began investigating divergent cusped-field (DCF) thrusters to determine their promise as a longer lifetime alternative to existing low power Hall thrusters. Other cusped-field thrusters include the High Efficiency Multi-stage Plasma (HEMP) thrusters patented by THALES Electron Devices[4–6] and the Cylindrical Hall Thruster (CHT) developed at the Princeton University Electric Propulsion & Plasma Dynamics Laboratory.[7] A detailed comparison of the DCFT design to the HEMP, CHT, and other cusped-field devices is provided by Courtney et al.[8]

A. Divergent Cusped-Field Thruster (DCFT)

DCF thrusters are electric propulsion devices characterized by a divergent, dielectric wall channel and a magnetic topology dominated by two magnetic cusps and a magnetic bottle near the anode. The magnetic circuit consists of three annular samarium cobalt (SmCo) permanent magnets arranged such that like poles face one another, and a core at the base of the thruster composed of 1018 carbon steel (see Figs. 1(a) and 1(b)). Xenon gas is injected 5 mm upstream from the downstream face of the anode through a porous, stainless steel disc embedded in the magnetic core. In this way, the neutral injection and anode locations are decoupled from one another in the DCFT design. For complete details of the DCFT and existing data, please consult previous studies.[8–13]

Existing experimental data[8–10] catalogues DCFT performance (anode specific impulse, thrust, anode thrust efficiency) at operating conditions ranging between 100 W to 500 W, with a nominal operating condition corresponding to a xenon flow rate of 8.5 sccm and an applied anode voltage of 550 V. At this operating point, the DCFT consumes 242 W of power, and produces 13.4 mN of thrust while operating with an anode thrust efficiency of 44.5%. Although basic DCFT operating principles are thought to include azimuthal electron currents within regions characterized by radial magnetic fields, the competing roles that strong magnetic bottles and internal electric fields play in determining the location and efficiency of ionization (whether in the upstream cusp, downstream cusp, or both) have not been measured in experiments or rigourously explained based on theoretical arguments or simulation results. Demonstrating the effectiveness of the magnetic topology and divergent chamber geometry as erosion barriers remains unachieved as well.

The 31st International Electric Propulsion Conference, University of Michigan, USA
September 20-24, 2009

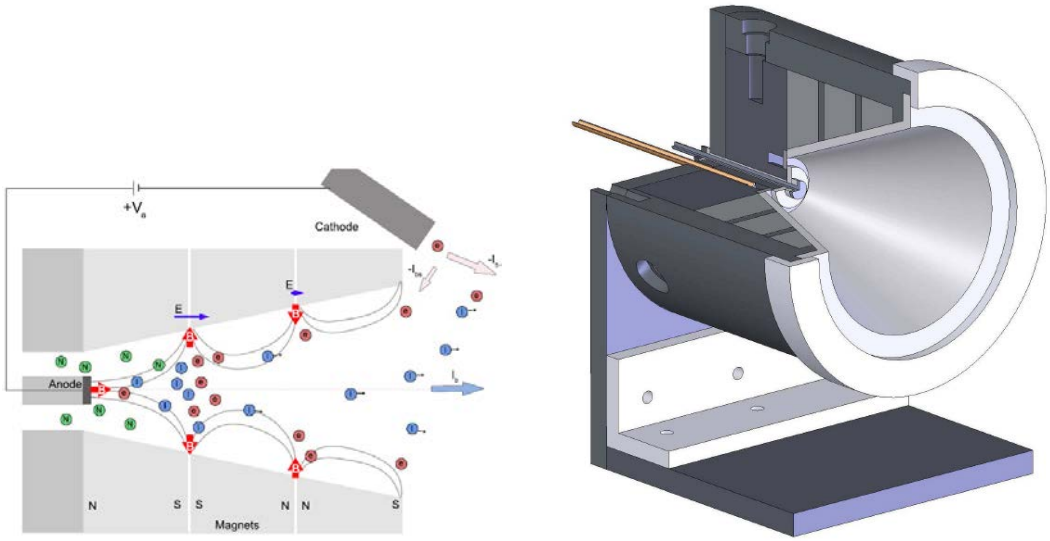

(a) DCFT schematic.[10] (b) 3D Engineering Model of DCFT.[9]

Figure 1. DCFT visualizations.

The present investigation provides detailed probing results of the DCFT plume using a Faraday cup (FC) and a retarding potential analyzer (RPA) to measure the ion current density and energy distributions of ion flux at different flow rates and applied voltages. FC and RPA results are presented for several operating conditions, including cases where the cathode flow and power were altered to study the affect of these changes on visible and measured plume structure. Anode current oscillation measurements are also given.

II. Plume Measurements

The following experiments were performed in Chamber 1 at the Edwards Air Force Base (AFB) Air Force Research Laboratory (AFRL) Space Propulsion Branch. Chamber 1 is a cylindrical, non-magnetic, stainless steel vacuum chamber with a 2.4 m diameter and a 4.1 m length. Pumping is provided by two liquid nitrogen baffled, 1.2 m flanged gaseous helium two stage cryogenic (15 K) vacuum pumps with a measured pumping speed on both xenon and krypton of 48,500 L/s. An automated 2D (R-Θ) stage was used to move Faraday and RPA probes within the plume of an operating DCF thruster to measure the characteristics of the plasma being ejected. The arm mounted on the rotary stage is a stepper motor drive linear translational stage capable of traversing up to 80 cm from the center of rotation of the rotary stage. This combination of rotary and linear motion allows for the continuous sweeping of plasma probes in the R-Θ plane. Further details of the experimental facilities are provided by Nakles et al.[14]

Figures 2(a) and 2(b) show the thruster firing at the Edwards AFB AFRL, and Fig. 3 illustrates the coordinate system used to present the probe data. The thruster was fired for a total of 18 hrs. during this investigation. Thermocouples located on the thruster exterior near the anode and outer case enclosing the permanent magnets indicate that the temperature did not exceed 200°C at those locations during all tests performed for this investigation. Measured chamber pressure did not exceed 3.5 μTorr. The cathode was positioned with the plasma orifice center located 27.5 mm $\pm$ 1 mm downstream of the exit plane and 31.8 mm $\pm$ 1 mm outside the maximum radius of the thruster at the exit plane, as in previous investigations.[8–10] Furthermore, the thruster body was electrically insulated from the chamber ground potential throughout all tests performed.

A. Current Density

This section contains Faraday cup results for selected operating conditions, plotted as current per steradian. The data are given in Figs. 5 through 8. The FC data points are angularly resolved from $\pm 120^o$ off axis in 1^o intervals in both directions, taken at two different radii from the thruster exit plane at each condition.

(a) DCFT operating in the high-current, or diffuse, mode.

(b) DCFT operating in the low-current mode.

Figure 2. A visual comparison of the DCFT plume in two distinct modes, operating at the Edwards AFB AFRL.

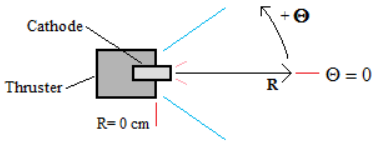

Figure 3. Top view of the 2D (R-Θ) coordinate system. The Θ = 0 line is aligned with the DCFT axis of symmetry. The cathode is above the probing plane, as seen is Figs. 2(a) and 2(b).

The Faraday cup used to measure current density is pictured in Fig. 4(b). Ion current is collected and measured on the inner disk, measuring 8.3 mm in diameter. A concentric guard piece, measuring 22.5 mm in outer diameter, is used to minimize the effects of the plasma sheath on the ion current collector's effective collecting area. The electrodes are constructed from molybdenum. A 0.56 mm wide gap exists between the outer wall of the collector and the inner wall of the guard ring. The effective current collector area of the probe is calculated by adding a portion of the gap surface area to the collector surface area as suggested in Ref. 15. Ion charge flux is determined by dividing the current to the collector by its effective surface area. The disk and guard ring are biased to -30.0 V with respect to chamber ground so that ion saturation is achieved. The effects of secondary electron emission are assumed to be less than a few percent[16] and are neglected in this analysis.

Figures 5 through 7 show Faraday cup data for the DCFT operating in the high current mode. The operating condition of the thruster in Fig. 5 is V_a = 300 V, $\dot{m}_a$ = 8.5 sccm, I_a = 0.53 A ± 0.03 A, I_k = 0.23 A, $\dot{m}_c$ = 1.0 sccm, and V_k = 16.8 V ± 0.6 V. Figure 6 shows the same measurements for a different operating condition: V_a = 450 V, $\dot{m}_a$ = 8.5 sccm, I_a = 0.58 A ± 0.03 A, I_k = 0.23 A, $\dot{m}_c$ = 1.0 sccm, and V_k = 16.4 V ± 0.5 V. The DCFT operating condition for the measurements presented in Fig. 7 is identical to that in Fig. 6, except that the keeper current is 0.23 A in Fig. 6 and 0.48 A in Fig. 7, I_a = 0.617 A ± 0.005 A, and V_k = 16.1 V ± 0.2 V. The uncertainties in the anode currents and keeper potentials represent the limits over which the values drifted during measurements, due in part to the thruster warming or cooling with changes in operating condition. The basic plume structure is identical in all three plots, showing a hollow plume with the maximum current density located between $30 \leq |\Theta| \leq 35$. The current density on the centerline of the thruster is about a factor of 2 lower than in the densest regions. Note the logarithmic scale of the vertical axes in Figs. 5 through 8. The current density also begins to increase past $|\Theta| > 80^o$ before decreasing again at larger angles. This is most likely due to charge exchange collisions with neutral particles. Repeating these measurements at varied chamber pressures would determine whether the ions are colliding with unionized xenon in the thruster flow, or with the background gas population of neutral particles within the vacuum chamber.

Figure 8 shows the current density per steradian for the DCFT operating in the low-current mode, with V_a = 475.7 V, $\dot{m}_a$ = 5.8 sccm, I_a = 0.1415 A ± 0.0015 A, I_k = 1.48 A, $\dot{m}_c$ = 1.0 sccm, and

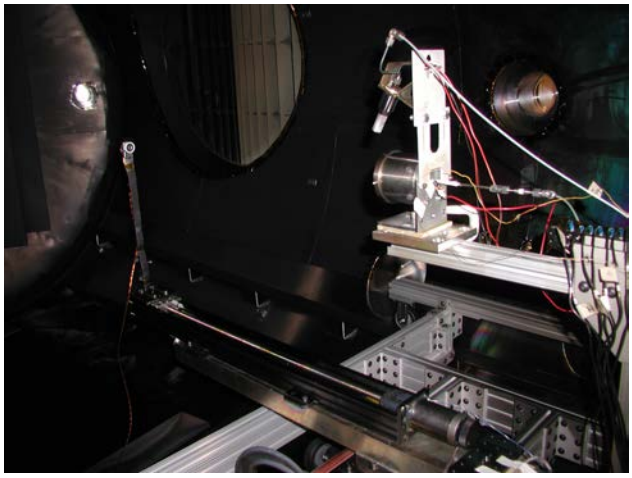

(a) Faraday cup mounted and aligned to measure current density within the DCFT plume.

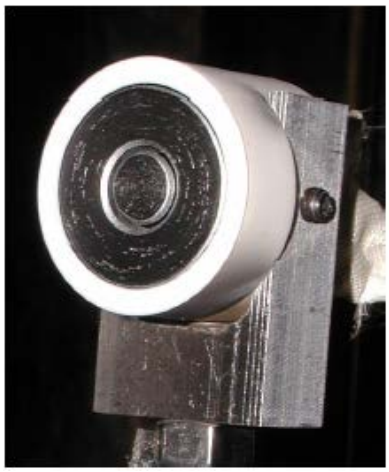

(b) Detail of the Faraday cup.

Figure 4. The Faraday cup used to record plume measurements.

V_k = 17.1 V ± 0.5 V. The anode current is much lower here than for the high-current mode, though the basic structure of the current density appears identical over a wide range of angles. The one exception is on the thruster centerline, where the current density is less than the maximum value seen between $30 \leq |\Theta| \leq 35$ by an order of magnitude, compared to the high-current mode, where the centerline current density dropped by only a factor of 2 compared to the maximum value. Although the data suggest that current densities on the centerline are reduced in the low-current mode relative to the high-current mode, the dissimilarities in the operating conditions between the two modes suggest that more plume probing of the thruster operating in the low-current mode is needed.

The beam current is determined by integrating current density for $0 \leq |\Theta| \leq 90$, which also allows the ninety percent current half angle ($\Theta_{90\%}$) to be determined. Values for each Faraday cup scan are given in the captions of Figs. 5 through 8. High-current conditions are characterized by lower ratios of beam to anode current, but higher ratios of beam to neutral current. The ion current corresponding to the complete ionization of 8.5 sccm is 0.614 A, and 0.419 A for 5.8 sccm. Additionally, the low-current condition shown in Fig. 8 has a more focused plume than the high-current cases. However, unlike in past studies,[8,9] the low-current mode could only be maintained long enough to complete probe sweeps by increasing the cathode keeper current in all tests performed for this investigation. Previously, increasing the anode potential was often sufficient to initiate the transition from the high to low-current mode. Subsequently, we are hesitant to draw conclusions related to the benefit of one mode over the other based on integrated current density analyses.

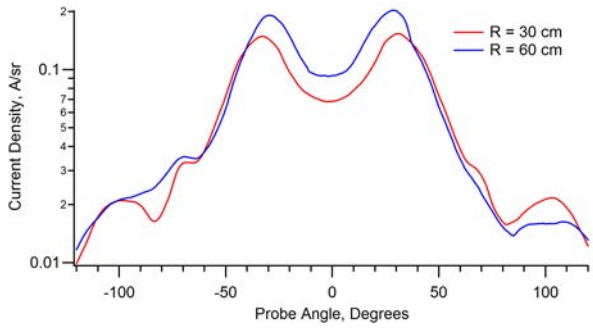

Figure 5. Ion current density distributions plotted at varying positions with respect to the DCFT exit plane. Operating condition: V_a = 300 V, $\dot{m}_a$ = 8.5 sccm, I_a = 0.53 A ± 0.03 A, I_k = 0.23 A, $\dot{m}_c$ = 1.0 sccm, V_k = 16.8 V ± 0.6 V; high-current mode. For R = 30 cm: I_b = 0.38 A, $\Theta_{90\%} = 72^o$; R = 60 cm: I_b = 0.43 A, $\Theta_{90\%} = 72^o$.

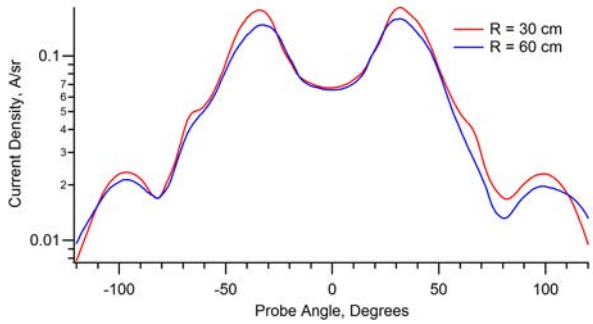

Figure 6. Ion current density distributions plotted at varying positions with respect to the DCFT exit plane. Operating condition: V_a = 450 V, $\dot{m}_a$ = 8.5 sccm, I_a = 0.58 A ± 0.03 A, I_k = 0.23 A, $\dot{m}_c$ = 1.0 sccm, V_k = 16.4 V ± 0.5 V; high-current mode. For R = 30 cm: I_b = 0.45 A, $\Theta_{90\%} = 70^o$; R = 60 cm: I_b = 0.40 A, $\Theta_{90\%} = 70^o$.

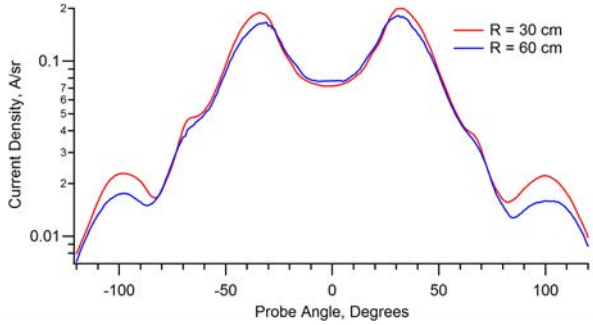

Figure 7. Ion current density distributions plotted at varying positions with respect to the DCFT exit plane. Operating condition: V_a = 450 V, $\dot{m}_a$ = 8.5 sccm, I_a = 0.617 A ± 0.005 A, I_k = 0.48 A, $\dot{m}_c$ = 1.0 sccm, V_k = 16.1 V ± 0.2 V; high-current mode. For R = 30 cm: I_b = 0.46 A, $\Theta_{90\%} = 70^o$; R = 60 cm: I_b = 0.43 A, $\Theta_{90\%} = 69^o$.

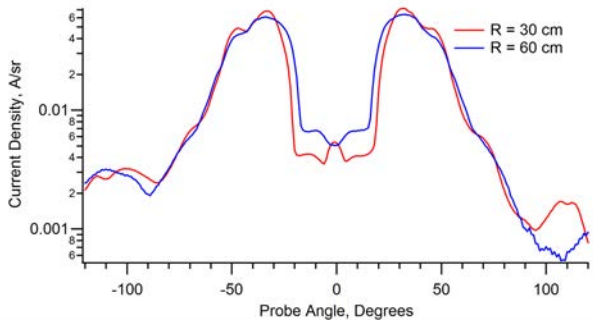

Figure 8. Ion current density distributions plotted at varying positions with respect to the DCFT exit plane. Operating condition: V_a = 475.7 V, $\dot{m}_a$ = 5.8 sccm, I_a = 0.1415 A ± 0.0015 A, I_k = 1.48 A, $\dot{m}_c$ = 1.0 sccm, V_k = 17.1 V ± 0.5 V; low-current mode. For R = 30 cm: I_b = 0.133 A, $\Theta_{90\%} = 61^o$; R = 60 cm: I_b = 0.135 A, $\Theta_{90\%} = 61^o$.

B. RPA Probing

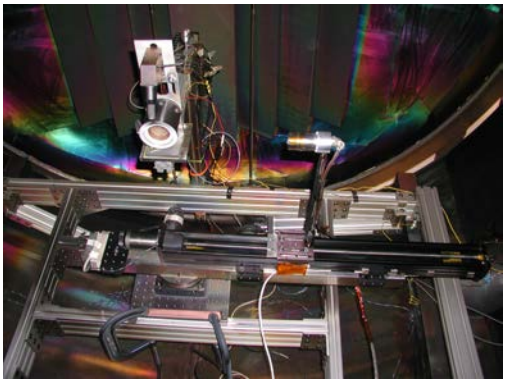

(a) RPA mounted and aligned to measure energy distributions of ion flux within the DCFT plume.

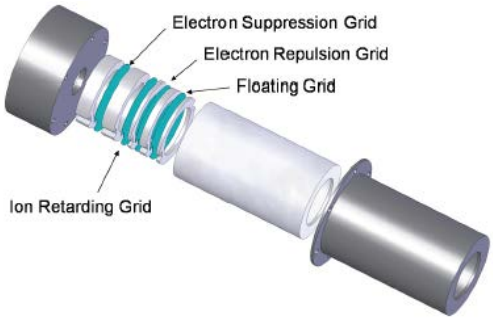

(b) Detail of the retarding potential analyzer.

Figure 9. The retarding potential analyzer used to record plume measurements.

This section presents RPA results for several different operating conditions, shown in Figs. 10(a) through 13(m). The RPA data are angularly resolved from $\pm 90^o$ or $\pm 120^o$ off axis in 5^o intervals in both directions, taken at two different radii from the thruster exit plane at each condition, except where indicated. The RPA used in this experimental investigation is shown in Fig. 9(b) and employs four grids. The floating grid potential remains at the local plasma potential and is meant to minimize probe effects within the plume. The electron repulsion grid, biased negatively with respect to chamber ground, repels incoming electrons while allowing ions to pass through. The potential of the ion retarding grid is swept positively relative to chamber ground to allow selective passage of ions based on their kinetic energy. The electron suppression grid is placed in front of the collector to suppress the electron current induced by ion impacts on the retarding grid. Reference 15 provides a more complete description of the RPA used in this investigation

As the ion retarding potential is increased from the ground potential to a specified limit, ions with lower energies are prevented from reaching the collector. The difference in ion currents measured between two distinct retarding potentials provides the portion ion flux comprised of ions with energies between the energies needed to overcome the retarding potentials. For appropriately small steps in retarding potential, the energy distribution of ion flux incident upon the RPA at a particular location is proportional to the negative of the derivative of the ion current with respect to the retarding potential, as seen in Eqs. 1 through 3. The minimum ion energy allowed to reach the RPA collector (ε_{min}) is assumed equal to the energy associated with the ion retarding potential (eV_r) in order to arrive at Eq. 3 from Eq. 2. The curve on the right-hand-side of Eq. 3 is plotted in Figs. 10(a) through 13(m) after being normalized such that the integral over the range of given retarding potentials is unity. Hence, the plots show the relative values of the energy distribution of ion flux at each specified location.

$$I = eA_p\Gamma_i \tag{1}$$

$$\Gamma_i\left(\varepsilon_{min}\right) \equiv \int_{\varepsilon_{min}}^{\infty} f_\Gamma\left(\varepsilon\right)\, d\varepsilon \tag{2}$$

$$f_\Gamma\left(eV_r\right) \propto -\frac{\mathrm{d}I}{\mathrm{d}V_r} \tag{3}$$

Figures 10(a) through 10(s) show RPA data for the DCFT operating in the high-current mode with $V_a = 300$ V, $\dot{m}_a = 8.5$ sccm, $I_a = 0.525$ A $\pm$ 0.005 A, $I_k = 0.25$ A, $\dot{m}_c = 1.0$ sccm, and $V_k = 15.4$ V $\pm$ 0.2 V. Data in Figs. 11(a) through 12(f) correspond to the DCFT operating in the high-current once again, but with $V_a = 450$ V, $\dot{m}_a = 8.5$ sccm, $I_a = 0.57$ A $\pm$ 0.05 A, $I_k = 0.25$ A, $\dot{m}_c = 1.0$ sccm, and $V_k = 15.7$ V $\pm$ 0.1 V. Figs. 12(a) - 12(f) show RPA data for angles outside of $\pm$ 90° at the same operating condition. Measurements at both operating conditions show energy distributions of ion flux for $0 \leq |\Theta| \leq 20$ with a mixture of high and low energy ions on the center line, transitioning toward a more monoenergetic distribution for $25 \leq |\Theta| \leq 50$, where a sharp peak is evident near the applied anode voltage. The most energetically uniform ion flux

distributions are located within regions of the plume that coincide with the greatest current densities, while centerline distributions are broader, comprised of both low and high energy ions. Between $55 \leq |\Theta| \leq 75$ distributions remain peaked just below the the anode voltage, though the number of low energy ions increases as compared to $25 \leq |\Theta| \leq 50$. At larger angles, for $80 \leq |\Theta| \leq 120$, the high energy peak disappears and is replaced by a broader, lower energy peak. Although the current density at these high angles is an order of magnitude less than the maximum, the energies of ions measured at high angles in the DCFT are greater than those measured in Hall thrusters.[17] Data identical to those shown in Figs. 11(a) through 12(f) were taken for the same operating condition, but with a keeper current of 0.50 A instead of 0.25 A. Doubling the keeper current at this operating condition had little or no effect on the RPA probe results, and are not presented here.

Figures 13(a) through 13(m) show RPA data for the DCFT operating in the low-current mode with $V_a = 451.5$ V, $\dot{m}_a = 4.3$ sccm, $I_a = 0.052$ A $\pm$ 0.009 A, $I_k = 1.98$ A, $\dot{m}_c = 2.0$ sccm, and $V_k = 16.55$ V $\pm$ 0.05 V. The operating condition for the low-current RPA data in Figs. 13(a) through 13(m) is not the same as the condition for FC data in Fig. 8. The energy distributions of ion flux are much different at this operating condition than for the conditions shown in Figs. 10(a) through 12(f). The degree to which these differences are attributable to the different modes or the varied operating conditions was not addressed in the present investigation. Nonetheless, ions exhibit strongly monoenergetic distributions between $30 \leq |\Theta| \leq 50$, as in the high-current mode. However, the relatively high energy ion populations present at large angles in the high-current mode are absent in the low-current mode examined here, except for $60 \leq |\Theta| \leq 70$. Instead for $0 \leq |\Theta| \leq 10$ and $80 \leq |\Theta| \leq 120$ the energy peaks of the flux distribution are much closer to energies that could be expected of initially slow ions that have been accelerated sideways by a potential hump along the beam.

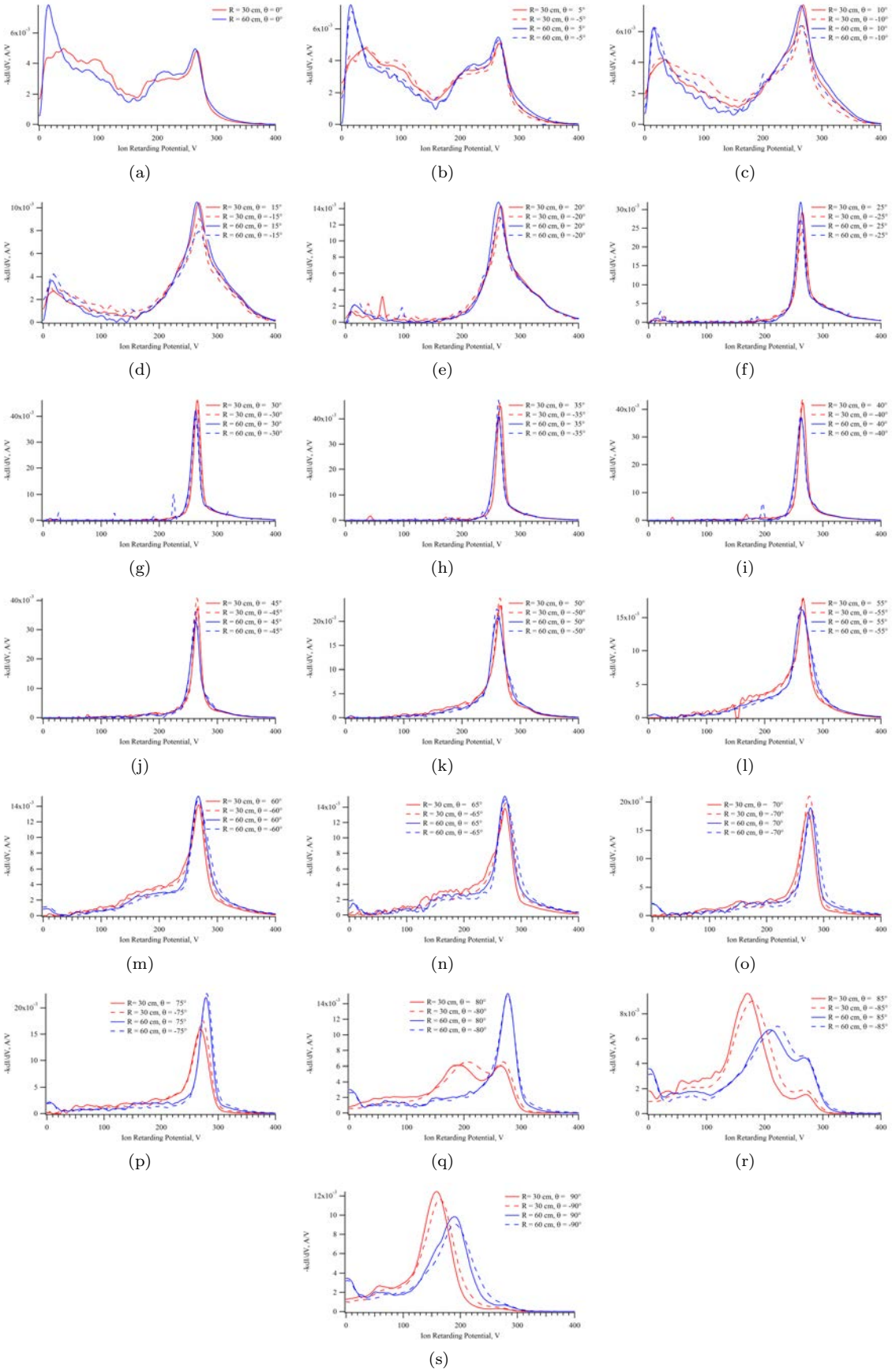

Figure 10. Ion energy distributions plotted at varying positions with respect to the DCFT exit plane. Operating condition: V_a = 300 V, $\dot{m}_a$ = 8.5 sccm, I_a = 0.525 A ± 0.005 A, I_k = 0.25 A and $\dot{m}_c$ = 1.0 sccm, V_k = 15.4 V ± 0.2 V

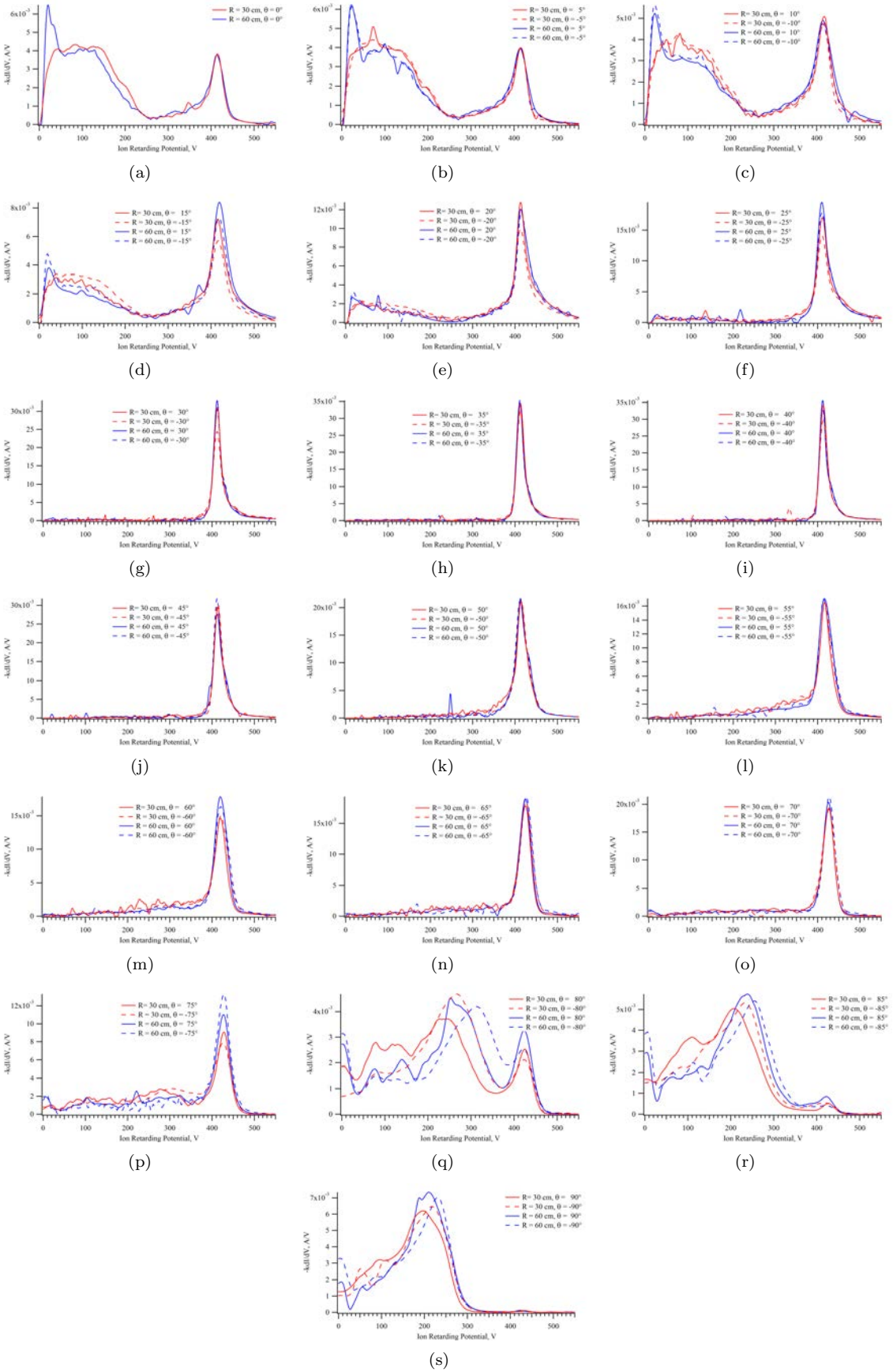

Figure 11. Ion energy distributions plotted at varying positions with respect to the DCFT exit plane. Operating condition: V_a = 450 V, $\dot{m}_a$ = 8.5 sccm, I_a = 0.57 A ± 0.05 A, I_k = 0.25 A and $\dot{m}_c$ = 1.0 sccm, V_k = 15.7 V ± 0.1 V.

The 31st International Electric Propulsion Conference, University of Michigan, USA
September 20-24, 2009

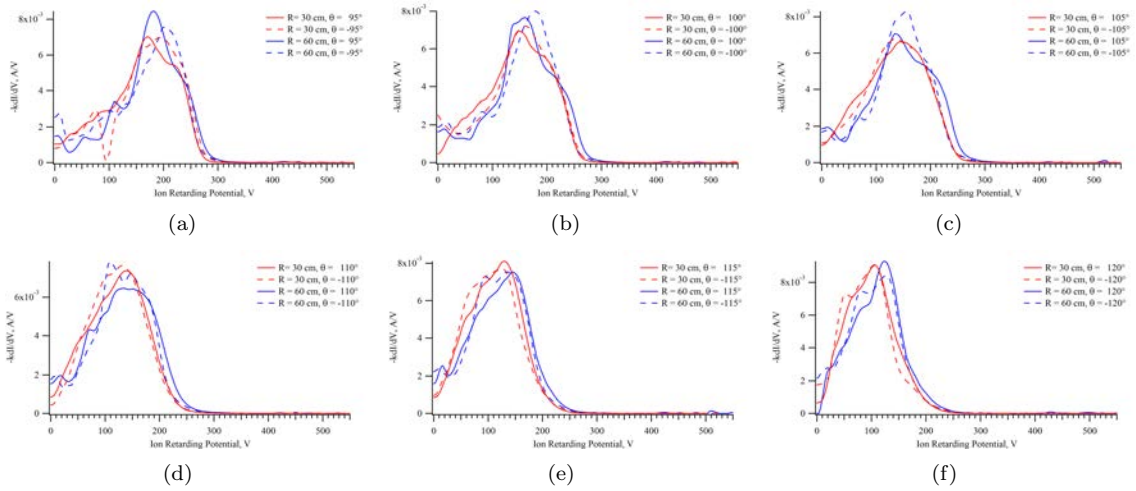

Figure 12. Ion energy distributions plotted at varying positions with respect to the DCFT exit plane. Operating condition: V_a = 450 V, $\dot{m}_a$ = 8.5 sccm, I_a = 0.57 A ± 0.05 A, I_k = 0.25 A and $\dot{m}_c$ = 1.0 sccm, V_k = 15.7 V ± 0.1 V. For angles inside of ± 90° at this operating condition, see Figs. 11(a) - 11(s).

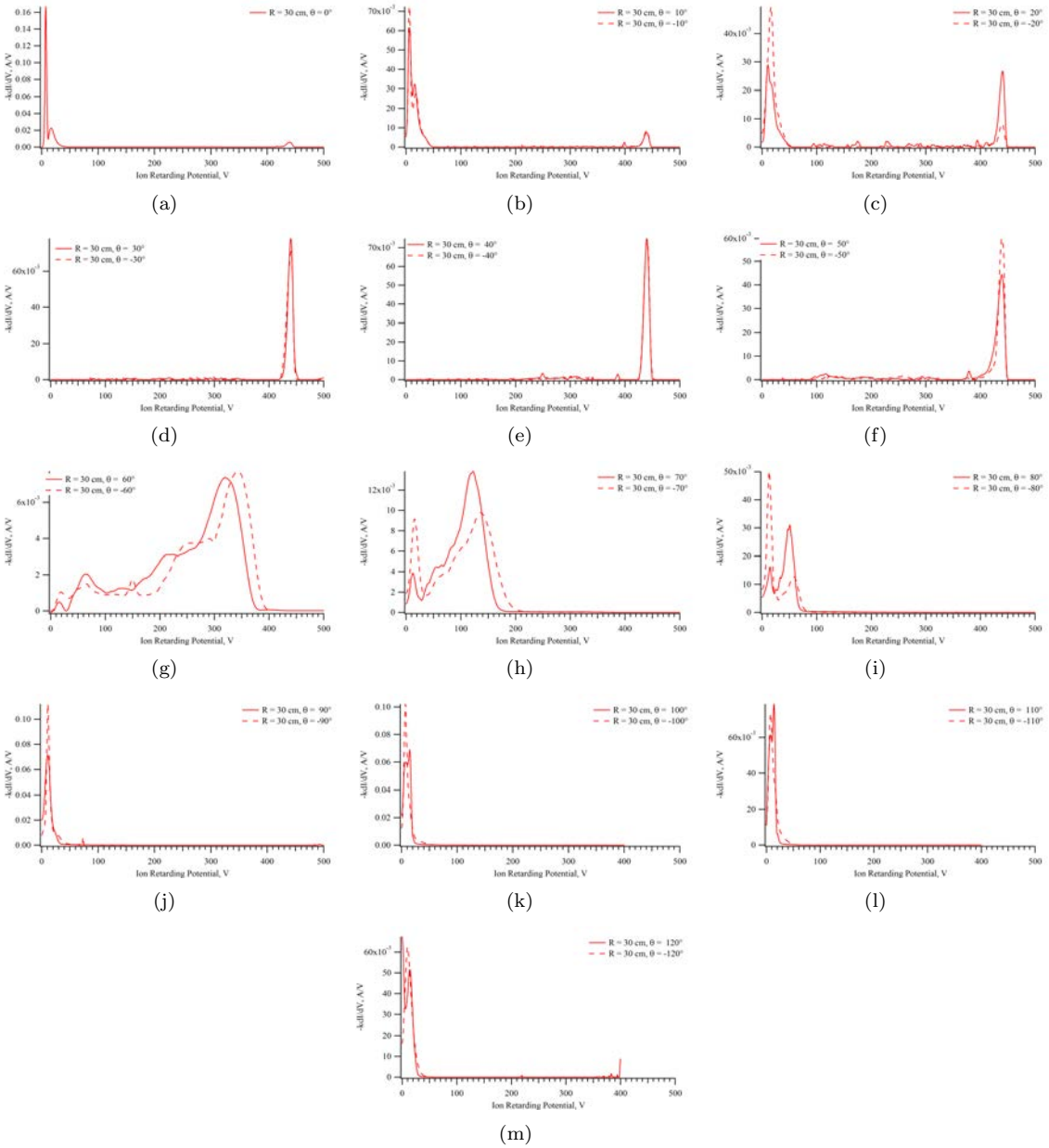

Figure 13. Ion energy distributions plotted at varying positions with respect to the DCFT exit plane. Operating at V_a = 451.5 V, $\dot{m}_a$ = 4.3 sccm, I_a = 0.052 A ± 0.009 A, I_k = 1.98 A, $\dot{m}_c$ = 2.0 sccm, V_k = 16.55 V ± 0.05 V.

The 31st International Electric Propulsion Conference, University of Michigan, USA
September 20-24, 2009

III. Current Oscillation Measurements

This section presents time resolved anode currents as recorded with an oscilloscope and processed with a signal analyzer. They demonstrate a conspicuous difference between the anode current behavior in the high and low-current modes. The anode currents shown in Figs. 14(a) through 14(f), representing the DCFT operating in the high-current mode, are characterized by high magnitude, low frequency oscillations. For all high-current operating conditions examined here, the lowest harmonic of the frequency spectrum is between 3.5 kHz and 4.0 kHz. The value of the lowest harmonic frequency appears to be unaffected by the operating condition of the thruster, in agreement with the theoretical frequency of highly nonlinear breathing modes in plasma discharges given by Barral and Ahedo.[18] They suggest that the frequency of current oscillation is approximately equal to the quotient of the neutral thermal speed and a characteristic thruster length. The residence time of a neutral xenon particle with a thermal speed corresponding to a temperature of 1000 K over the 5 cm axial length of the DCFT is approximately 0.2 ms. The frequency corresponding to the inverse of this time is 5 kHz, in close agreement with the lowest harmonic frequency of anode current oscillations for the DCFT operating in the high-current mode.

The anode currents shown in Figs. 15(a) through 15(f), representing the DCFT operating in the low-current mode, do not exhibit the same oscillatory behavior as seen in the high-current mode. The large oscillations present in the high-current mode are reduced by several orders of magnitude. The narrow dispersion of ion energies in Figs. 13(a) through 13(m) within regions of maximum current density in Fig. 8 may account for the lack of strong oscillations in the low-current mode, as laser-induced fluorescence studies of Hall thrusters have shown.[19] Previously,[9,10] the low-current mode was found to be the more efficient of the two modes. The lack of strong plasma oscillations in the low-current mode further suggest that it is the preferred mode of operation.

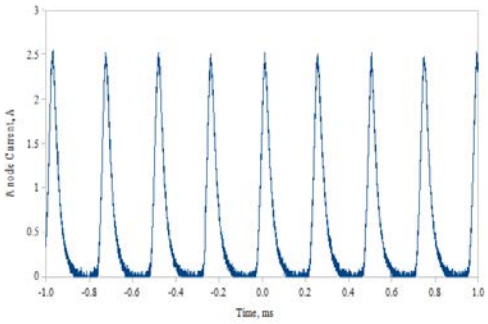

(a) Time resolved anode current. The thruster operating condition for these data is identical to Fig. 5

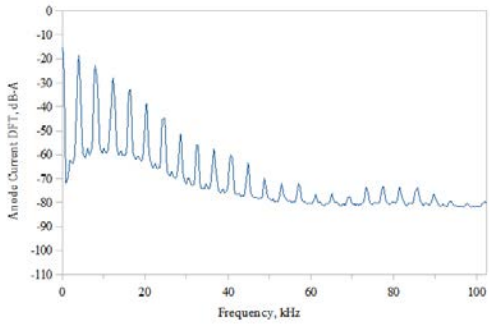

(b) Anode current spectrum. The thruster operating condition for these data is identical to Fig. 5

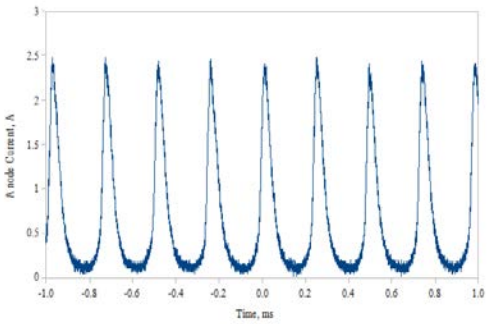

(c) Time resolved anode current. The thruster operating condition for these data is identical to Fig. 6

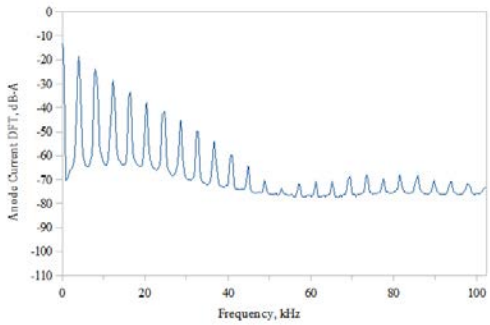

(d) Anode current spectrum. The thruster operating condition for these data is identical to Fig. 6

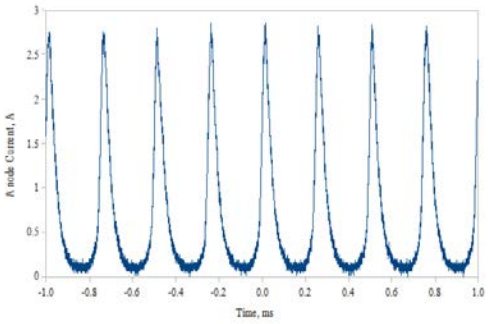

(e) Time resolved anode current. The thruster operating condition for these data is identical to Fig. 7

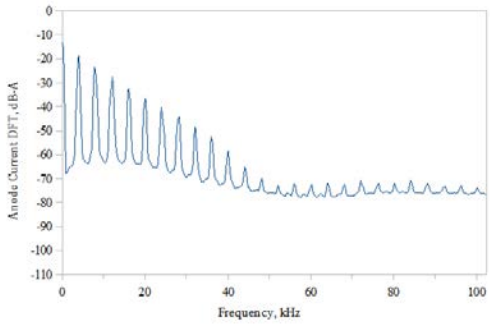

(f) Anode current spectrum. The thruster operating condition for these data is identical to Fig. 7

Figure 14. Time resolved anode currents and spectrum for the high-current mode.

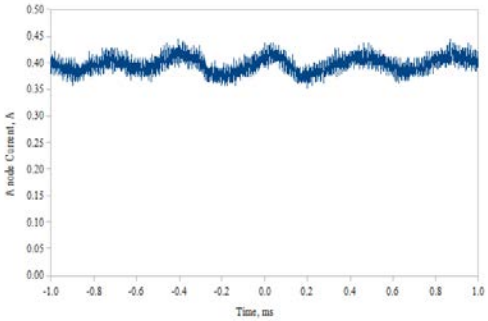

(a) Time resolved anode current. Operating condition is identical to Fig. 7. These data were recorded while the thruster warmed, after which it transitioned to the high-current mode, as in Fig. 14(e).

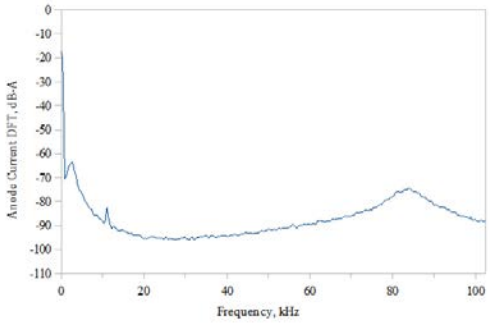

(b) Time resolved anode current. These data were recorded while the thruster warmed up, after which it transitioned to the high-current mode, as in Fig. 14(f).

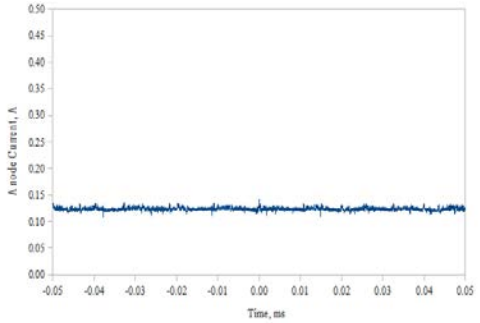

(c) Time resolved anode current. The thruster operating condition for these data is identical to Figs. 13(a) through 13(m).

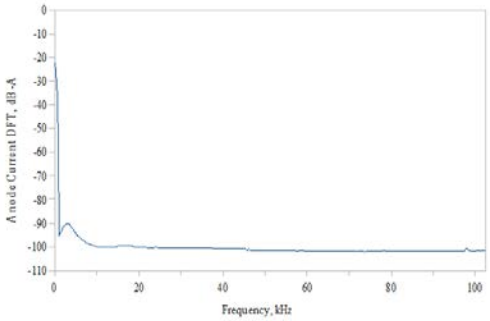

(d) Time resolved anode current. The thruster operating condition for these data is identical to Figs. 13(a) through 13(m).

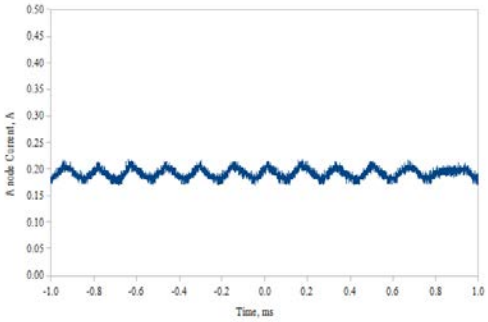

(e) Time resolved anode current. The thruster operating condition for these data is identical to Fig. 8.

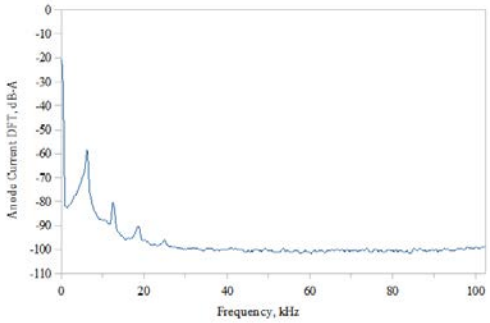

(f) Time resolved anode current. The thruster operating condition for these data is identical to Fig. 8.

Figure 15. Time resolved anode currents and spectrum for the low-current mode.

The 31st International Electric Propulsion Conference, University of Michigan, USA
September 20-24, 2009

IV. Conclusion

The plume measurements expand upon and confirm previous RPA and Faraday cup data.[8,9] A comparison of RPA and Faraday data for identical operating conditions shows that the region of the plume with the greatest current density contains the most energetically uniform ion populations. However, the RPA results indicate that highly energetic ions are expelled at large angles relative to the DCFT axis of symmetry, though the current densities at these angles are much lower. Time resolved anode current data reveal a distinct difference between the low and high-current modes. The data demonstrate that the anode current in the low-current mode is much less oscillatory than in the high-current mode. Identifying the cause of this difference in dynamic behavior will likely contribute toward the determination of basic DCFT operating principles in each mode.

While running the thruster for the purpose of this investigation, the operating conditions of the DCFT and cathode were found to be strongly coupled, motivating a future study that systematically examines the effect of cathode location and operating condition on the performance of the DCFT. A detailed look at the ion energy distributions at high angles in the low-current mode would also be beneficial, to determine if high energy ions are as prevalent at high angles in the low-current as in the high-current mode. Additionally, repeating some of the measurements made here at different chamber pressures would address the role that charge exchange collisions with background neutrals play in deflecting ions to high angles. However, it is likely that the strong magnetic field outside the thruster is a strong contributor to the high ion energies observed at large plume angles.

Acknowledgments

Paul Adkinson, of the Edwards AFB AFRL, was immensely helpful in the construction, assembly and repair of the anodes used in these experiments. The authors would also like to acknowledge Ryne Barry, an undergraduate student in the Department of Aeronautics & Astronautics at the Massachusetts Institute of Technology, for his assistance in experimental setup and execution. The authors would also like to acknowledge the Science Mathematics And Research for Transformation (SMART) scholarship program for the funding and opportunities that made this project possible. Continuing studies of the divergent cusped-field thruster concept are funded by a grant from the Air Force Office of Scientific Research.

References

[1]Bober, A. S., Kim, V., et al., "State of Works on Electrical Thrusters in the USSR," 22^{nd} *International Electric Propulsion Conference*, Viareggio, Italy, October 1991, also IEPC-91-003.

[2]Martínez-Sánchez, M. and Pollard, J. E., "Spacecraft Electric Propulsion - An Overview," *Journal of Propulsion and Power*, Vol. 14, No. 5, 1998, pp. 688–699.

[3]Kim, V., "Main Physical Features and Processes Determining the Performance of Stationary Plasma Thrusters," *Journal of Propulsion and Power*, Vol. 14, No. 5, 1998, pp. 736–743.

[4]Kornfeld, G., Koch, N., and Coustou, G., "First Test Results of the HEMP Thruster Concept," 28^{th} *International Electric Propulsion Conference*, Toulouse, France, March 2003, also IEPC–03–134.

[5]Kornfeld, G., "Plasma Accelerator Arrangement," United States Patent 6,523,338 B1, 2003.

[6]Kornfeld, G., Coustou, G., and Emsellem, G., "Plasma Accelerator System," United States Patent 7,075,095 B2, 2006.

[7]Raitses, Y. and Fisch, N. J., "Parametric Investigations of a Nonconventional Hall Thruster," *Physics of Plasmas*, Vol. 8, No. 5, 2001.

[8]Courtney, D., Lozano, P., and Martínez-Sánchez, M., "Continued Investigation of Diverging Cusped Field Thruster," 44^{th} *Joint Propulsion Conference & Exhibit*, Hartford, CT, July 2008, also AIAA-2008-4631.

[9]Courtney, D. G., "Development and Characterization of a Diverging Cusped Field Thruster and a Lanthanum Hexaboride Hollow Cathode," S.M. Thesis, Massachusetts Institute of Technology, Cambridge, MA, June 2008.

[10]Courtney, D. G. and Martínez-Sánchez, M., "Diverging Cusped-Field Hall Thruster (DCHT)," 30^{th} *International Electric Propulsion Conference*, FLorence, Italy, September 2007, also IEPC-2007-39.

[11]Matlock, T. et al., "Spectroscopic and Electrostatic Investigation of the Diverging Cusped-Field Thruster," 45^{th} *Joint Propulsion Conference & Exhibit*, Denver, Co, August 2009, also AIAA-2009-4813.

[12]Gildea, S., Batishchev, O., and Martínez-Sánchez, M., "Fully Kinetic Modeling of Divergent Cusped-Field Thrusters," 45^{th} *Joint Propulsion Conference & Exhibit*, Denver, Co, August 2009, also AIAA-2009-4814.

[13]Gildea, S., "Fully Kinetic Modeling of a Divergent Cusped Field Thruster," M. Sc. Thesis Project, Massachusetts Institute of Technology, Cambridge MA, May 2009.

[14]Nakles, M., Barry, R., Larson, C. W., and Hargus, W. A., "A Plume Comparison of Xenon and Krypton Propellant on a 600 W Hall Thruster," 31^{st} *International Electric Propulsion Conference*, Ann Arbor, MI, September 2009.

[15]Brown, D. L., "Investigation of Low Discharge Voltage Hall Thruster Characteristics and Evaluation of Loss Mechanisms," Ph.D. Thesis, University of Michigan, Ann Arbor, MI, 2009.

[16]Brown, S. C., *Basic Data of Plasma Physics*, American Institute of Physics Press, 1994.

[17]Azziz, Y., "Experimental and Theoretical Characterization of a Hall Thruster Plume," Ph.D. Thesis, Massachusetts Institute of Technology, Cambridge, MA,, 2007.

[18]Barral, S. and Ahedo, E., "Low-frequency model of breathing oscillations in Hall discharges," *Physical Review E*, Vol. 79, 2009.

[19]Hargus, W. A., Nakles, M. R., Tedrake, R., and Pote, B., "Effect of Anode Current Fluctuations on Ion Energy Distributions within a 600 W Hall Effect Thruster," 44^{th} *Joint Propulsion Conference & Exhibit*, Hartford, CT, July 2008, also AIAA-2008-4724.